



Cite this: DOI: 10.1039/d5el00071h

# Fluorinated fullerene interlayers for tin halide perovskite solar cells with enhanced operational air stability and minimized voltage losses†

Sergio Galve-Lahoz,<sup>ab</sup> Jesús Sánchez-Díaz,<sup>a</sup> Jorge Marco-Guimbao,<sup>b</sup> Nihal Guenani,<sup>a</sup> Jorge Simancas,<sup>ib</sup> Jhonatan Rodríguez-Pereira,<sup>ibcd</sup> Jesús Lucía-Tamudo,<sup>e</sup> Sergio Díaz-Tendero,<sup>ibfgh</sup> Jorge Pascual,<sup>b</sup> Beatriz Julián-López,<sup>ib</sup> Juan P. Martínez-Pastor,<sup>ib</sup> Eva M. Barea,<sup>a</sup> Iván Mora-Seró<sup>ib\*</sup> and Juan Luis Delgado<sup>ib\*bj</sup>

Tin halide perovskite solar cells (Sn-PSCs) are a promising alternative to their lead-based analogues due to their favorable optoelectronic properties. However, their performance is still limited by two main factors: on one hand, the tendency of  $\text{Sn}^{2+}$  to oxidize to  $\text{Sn}^{4+}$ , which leads to high non-radiative recombination; and on the other hand, the offset between the perovskite conduction band and the LUMO level of the standard  $\text{C}_{60}$  fullerene, which hinders efficient charge transport and limits overall device performance. While the former has received significant attention, the latter has been less explored, despite being a major bottleneck for Sn-PSC development. In this work, we designed and synthesized two novel fullerene derivatives, namely **JM10** and **JM12**, functionalized with different fluorine-rich moieties and incorporated them as interlayers between the perovskite and the  $\text{C}_{60}$  electron transport layer (ETL). These derivatives demonstrated suitable LUMO levels and effectively alleviated the energy level misalignment at the perovskite/ETL interface, minimizing the undesirable charge recombination and enhancing the charge extraction processes. As a result, the best-performing Sn-PSCs incorporating **JM12** showed a nearly 20% increase in power conversion efficiency with respect to the reference devices. Moreover, the fluorinated groups increased the hydrophobicity of the interlayers, significantly improving the operational stability of the unencapsulated devices under harsh ambient conditions (60% RH and 25 °C). As a result, devices containing **JM10** and **JM12** retained up to 80% of their initial performance after more than 15 and 18 hours, respectively. These results highlight the potential of fullerene chemistry's versatility to mitigate carrier losses at the interfaces while simultaneously improving both the performance and stability of Sn-PSCs, paving the way for future advancements in their design and development.

Received 6th May 2025  
Accepted 28th June 2025

DOI: 10.1039/d5el00071h

rsc.li/EESolar

<sup>a</sup>Institute of Advanced Materials (INAM), University Jaume I, Av. Vicent Sos Baynat, s/n, 12071, Castellón de la Plana, Spain. E-mail: sero@uji.es

<sup>b</sup>Polymat, University of the Basque Country UPV/EHU, 20018 Donostia-San Sebastian, Spain. E-mail: juanluis.delgado@polymat.eu

<sup>c</sup>Center of Materials and Nanotechnologies, Faculty of Chemical Technology, University of Pardubice, nám. Cs. legii 565, Pardubice, 53002, Czech Republic

<sup>d</sup>Central European Institute of Technology, Brno University of Technology, Purkynova 123, Brno, 602 00, Czech Republic

<sup>e</sup>Faculty of Chemistry and Pharmacy, Institute of Physical and Theoretical Chemistry, University of Regensburg, 93040 Regensburg, Germany

<sup>f</sup>Department of Chemistry, Universidad Autónoma de Madrid, 28049, Madrid, Spain

<sup>g</sup>Institute for Advanced Research in Chemistry (IAdChem), Universidad Autónoma de Madrid, 28049 Madrid, Spain

<sup>h</sup>Condensed Matter Physics Center (IFIMAC), Universidad Autónoma de Madrid, 28049 Madrid, Spain

<sup>i</sup>Instituto de Ciencia de los Materiales (ICMUV), Universitat de Valencia, 46980 Paterna, Spain

<sup>j</sup>Ikerbasque, Basque Foundation for Science, Bilbao 48013, Spain

† Electronic supplementary information (ESI) available. See DOI: <https://doi.org/10.1039/d5el00071h>

## Broader context

Since their emergence in 2009, lead-halide perovskite solar cells (PSCs) have shown great promise for high-efficiency, low-cost photovoltaics. However, concerns over lead toxicity have prompted efforts to develop safer alternatives. Tin-based perovskites (Sn-PSCs) stand out due to their favorable optoelectronic properties, but their efficiency and long-term stability still lag behind, largely due to suboptimal energy level alignment with standard electron transport materials like  $\text{C}_{60}$ . While alternatives such as ICBA have improved photoconversion efficiency (PCE), they often compromise device stability. This work targets a key limitation in Sn-PSC performance by developing two novel fluorinated fullerene derivatives, **JM10** and **JM12**, designed to improve energy alignment at the perovskite interface. Their incorporation as interlayers significantly enhances charge extraction, leading to PCE improvements of nearly 20%, and a sixfold increase in ambient stability for unencapsulated devices. These results represent an important step forward for lead-free PSCs, offering a promising route to safer and more stable solar energy technologies.



## Introduction

Since the first reported hybrid lead-halide perovskite solar cell (Pb-PSC) in 2009,<sup>1</sup> these materials have shown an unprecedented potential to outperform conventional silicon-based solar cells and dominate the photovoltaic market.<sup>2–4</sup> However, global regulations on lead as a hazardous material could hinder their commercialization.<sup>5–7</sup> To overcome this issue, the scientific community started to focus on alternative materials, with Sn demonstrating to be the best candidate to replace Pb at the divalent cation site due to its outstanding optoelectronic properties.<sup>8,9</sup> Nevertheless, the current record efficiencies achieved in Sn-PSCs still lag too far below the Shockley–Queisser theoretical limit efficiency ( $\sim 33\%$ ).<sup>10–13</sup>

One of the main reasons behind this efficiency gap is related to the poor band alignment between the conduction band (CB) of the Sn-perovskite active layer and the lowest unoccupied molecular orbital (LUMO) level of the commonly used C<sub>60</sub> ETL.<sup>14,15</sup> Initially, C<sub>60</sub> emerged as an effective ETL in Pb-PSCs due to its high charge mobility,<sup>16,17</sup> but the shallower CB of Sn-PSCs leads to the aforementioned energy mismatch. Accordingly, inefficient charge extraction at the interface and serious open-circuit voltage ( $V_{OC}$ ) losses are usually observed.<sup>14</sup> Nonetheless, the mixed  $sp^2$  and  $sp^3$  hybridization of the carbon atoms within the C<sub>60</sub> cage not only confers high charge mobility to the layer,<sup>18,19</sup> but also offers the possibility of raising the LUMO level of fullerene derivatives by disrupting their conjugated  $\pi$  systems through suitable cage functionalization.<sup>20–22</sup> This tunability has enabled the successful incorporation of alternative fullerene derivatives, such as phenyl-C<sub>61</sub>-butyric acid methyl ester (PCBM) or indene-C<sub>60</sub> bisadduct (ICBA), into Sn-PSCs as ETLs, yielding impressive  $V_{OC}$  values approaching the Shockley–Queisser theoretical limit.<sup>11,23–25</sup> However, reducing the conjugation within the cage notably decreases the electron mobility of the devices, thereby compromising the short circuit current density ( $J_{SC}$ ). For instance, Liang *et al.* studied different ETLs, including C<sub>60</sub>, PCBM and ICBA, in Pb-PSCs, and reported a significant decrease in the electron mobility across the fullerene layer, following the trend C<sub>60</sub> > PCBM > ICBA ( $1.6\text{ cm}^2\text{ V}^{-1}\text{ s}^{-1}$  for C<sub>60</sub>,  $6.1 \times 10^{-2}\text{ cm}^2\text{ V}^{-1}\text{ s}^{-1}$  for PCBM, and  $6.9 \times 10^{-3}\text{ cm}^2\text{ V}^{-1}\text{ s}^{-1}$  for ICBA), which subsequently influenced the  $J_{SC}$  of the devices.<sup>17</sup> Based on these observations, a promising strategy to address the energy level mismatch in Sn-PSCs, without leaving aside the excellent charge mobility offered by the C<sub>60</sub> ETL, involves the incorporation of novel fullerene derivatives with appropriate LUMO levels as interlayers between the perovskite active layer and the advantageous C<sub>60</sub>.<sup>15,26,27</sup>

Another critical issue in Sn-PSCs lies in the fast oxidation of Sn<sup>2+</sup> to the Sn<sup>4+</sup> state in the presence of oxidizing agents, such as water or oxygen molecules, leading to device instability and posing serious issues for the reliable study and processing of these materials.<sup>28,29</sup> To mitigate these degradation pathways, an interesting approach involves the development of new materials capable of physically isolating the perovskite layer without disrupting its electronic properties. In this context, fluorinated compounds have proven to be excellent moisture barriers due to

their high hydrophobicity, significantly enhancing the air stability of different Pb-PSCs.<sup>30–32</sup> Furthermore, the strong electronegativity of fluorine atoms allows them to interact with electron-deficient sites, such as I<sup>−</sup> vacancies, compensating charge deficiencies at the perovskite surface.<sup>33,34</sup> However, despite these promising characteristics, the potential of fluorinated compounds in Sn-PSCs remains largely unexplored, presenting a significant opportunity for future research.<sup>35,36</sup>

Herein, we decided to leverage the chemical versatility of fullerenes, which can be tailored with different functional groups to achieve desirable chemical and electronic properties. Specifically, we designed and synthesized two novel fullerene derivatives functionalized with different fluorine-rich moieties, namely **JM10** and **JM12**, and incorporated them as interlayers in Sn-PSCs. These interlayers optimized the energy level alignment between the CB of the perovskite and the LUMO level of C<sub>60</sub>, as we characterized experimentally and theoretically, boosting the  $V_{OC}$  and raising the power conversion efficiency (PCE) of the devices. In this way, **JM10** with a pentafluorobenzene unit showed an increased in the device efficiency to 10.5%, while **JM12** incorporated a 3,5-bis(trifluoromethyl)phenyl group and further boosted the efficiency to 11.0%, compared to 9.4% for the control devices, representing a 17% increase of performance. Furthermore, unencapsulated devices incorporating the interlayers presented an enhanced operational stability in air (60% RH and 25 °C), retaining up to 80% of their initial PCE after more than 15 and 18 hours of continuous operation for **JM10** and **JM12** fullerenes, respectively, while the control devices degraded after 3 hours of operation.

## Results and discussion

In this study, we designed and synthesized two novel [60]fulleropyrrolidines through a one-step 1,3-dipolar cycloaddition of different azomethine ylides to the C<sub>60</sub> precursor, that have been also theoretically simulated, see below. This reaction, also known as Prato reaction,<sup>37,38</sup> is widely used for the functionalization of fullerenes, as it allows for the straightforward attachment of different substituents to the fullerene cage. [60]Fulleropyrrolidines usually exhibit lower electron affinity than pristine C<sub>60</sub> fullerene or other derivatives, a property directly correlated with higher LUMO values.<sup>20,39,40</sup> As Sn-based perovskites present shallower CBs than their Pb-based counterparts, [60]fulleropyrrolidines are perfect candidates for fixing the inadequate band alignment at this interface.<sup>41</sup> Furthermore, both fullerene derivatives were functionalized with different fluorinated aromatic rings, and an *n*-butyl alkyl chain attached to the N atom of the pyrrolidine moiety. We anticipated that the fluorinated rings would enhance the hydrophobicity and the dipolar moment of the layer, thereby ensuring a better electron extraction, while the alkyl chain would increase the solubility of the fullerenes in non-polar solvents such as chlorobenzene. In this way, **JM10** presented a pentafluorophenyl unit and **JM12** incorporated a 3,5-bis(trifluoromethyl)phenyl group. The synthetic route is depicted in Scheme S1,<sup>†</sup> and the molecular structures are confirmed through nuclear magnetic resonance (<sup>1</sup>H NMR, <sup>13</sup>C NMR and <sup>19</sup>F NMR) and mass spectrometry (MS),



see Fig. S1–S8.† Further synthetic details are provided in the ESI.†

To evaluate the suitability of the synthesized materials, and their effectiveness to improve the charge extraction from the perovskite to the ETL, cyclic voltammetry (CV) experiments were conducted to determine their LUMO energy levels. The comparison of CV spectra is presented in Fig. 1a, where both **JM10** and **JM12** exhibited lower electron-accepting abilities compared to  $C_{60}$ , as indicated by their more negative half-wave potential values. The LUMO energy levels were estimated to be  $-4.05$  eV,  $-3.98$  eV and  $-4.01$  eV for  $C_{60}$ , **JM10** and **JM12**, respectively. The higher LUMO levels observed in both fullerene derivatives demonstrated their potential to enhance the charge extraction from the perovskite's CB to the ETL selective contact in Sn-PSCs. Additionally, the optical properties of the fullerene derivatives were analyzed using UV-vis absorption spectroscopy, see Fig. 1b. Fullerenes typically exhibit strong absorptions in the UV region, below 350 nm, associated to the typical  $\pi$ – $\pi^*$  transitions in aromatic systems.<sup>42</sup> The sharp peak at 430 nm observed for both **JM10** and **JM12** is attributed to the saturation of a double bond in the fullerene cage, confirming the formation of a 58  $\pi$ -electron system.<sup>43</sup> Moreover, both **JM10** and **JM12** presented a notorious redshift compared to pristine  $C_{60}$ , see inset in Fig. 1b, which is ascribed to the extended overall  $\pi$ -conjugation along the pyrrolidine and fluorinated moieties.<sup>44</sup> As

a result, a reduction in the energy gaps between the HOMO and the LUMO levels was obtained. The bandgaps  $E_g$  were estimated from the onset of the absorption, and the HOMO levels were calculated from  $E_{\text{HOMO}} = E_{\text{LUMO}} - E_g$ . All the parameters are summarized in Table S1† and the estimated energy levels are represented in Fig. 1c.

To elucidate the differences in the molecular electronic distribution between both derivatives, we analyzed their electrostatic potential (ESP) distributions and calculated their dipole moments using density functional theory (DFT). The properties of the  $C_{60}$  fullerene and two hypothetical intermediate derivatives, **JM8** and **JM9**, which progressively resemble the complexity of **JM10** and **JM12**, were also investigated to better understand the contributions of the different molecular components within their structure, see Fig. 1d. Due to the high icosahedral symmetry,  $I_h$ , of  $C_{60}$ , its net dipole moment,  $|\mu|$ , is zero. However, the spatially extended electron cloud of  $C_{60}$  fullerene enhances its molecular polarizability, owing to degenerated, energetically accessible LUMO orbitals that readily accept electrons. These characteristics enable strong polarization upon the incorporation of electron-donating or electron-withdrawing groups, leading to the formation of intense permanent molecular dipoles. Thereby, as shown in Fig. 1d and Table S2,† the addition of an *N*-methyl pyrrolidine moiety to the  $C_{60}$  unit leads to the hypothetical **JM8** molecule,

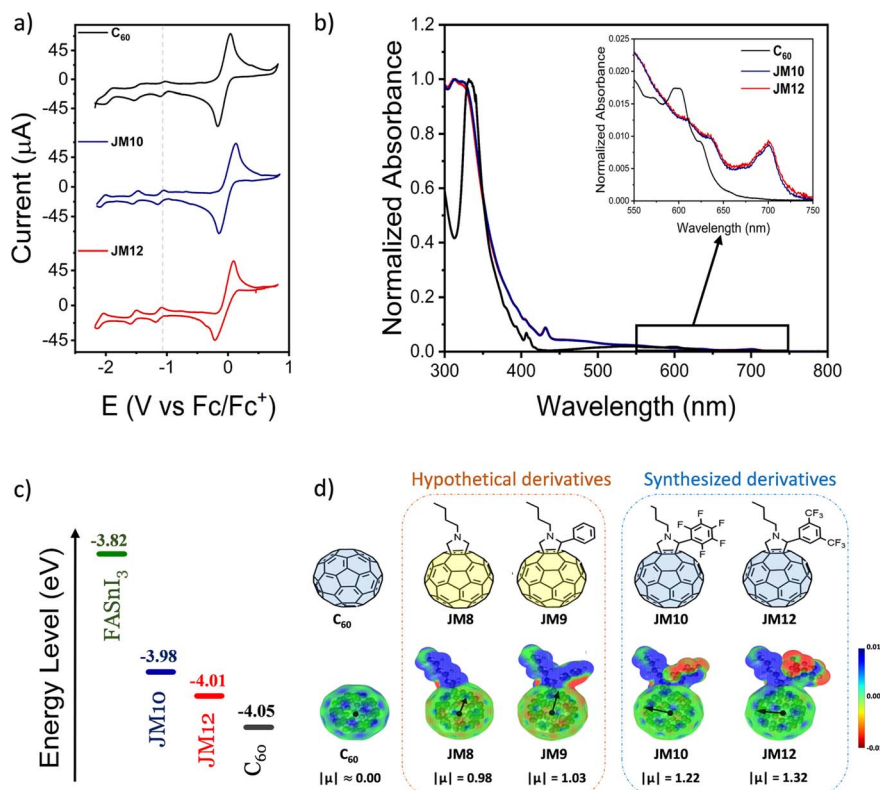


**Fig. 1** (a) CV of  $C_{60}$ , **JM10**, and **JM12** in acetonitrile : *o*-dichlorobenzene (1 : 4) ( $\text{NBu}_4^+\text{PF}_6^-$  0.1 M was employed as supporting electrolyte) vs.  $\text{Fc}/\text{Fc}^+$  couple, dotted line is an eye guide. (b) UV-vis absorption spectra of the fullerene derivatives in chlorobenzene ( $1 \times 10^{-5}$  M). (c) Schematic illustration of the LUMO levels for the different fullerene derivatives, extracted from (a) and conduction band of  $\text{FASnI}_3$  perovskite, extracted from ref. 45. (d) Molecular electrostatic potential at  $\rho = 0.001$  a.u. Range of values of the electrostatic potential: from  $-0.01$  (red) to  $0.01$  (blue). Black arrows indicate the net dipole moment direction.



which exhibits enhanced molecular polarization and a net dipole moment oriented along the direction of the substituent. This behavior arises from the electron-donating nature of the substituent, which increases the electronic density within the fullerene core (negative pole), while generating a positive pole at the substituent. Further functionalization with an aromatic ring yields **JM9** molecule, featuring a slightly intensified dipole along the same direction, due to the additional group's electron-donating effect. Interestingly, replacing all hydrogen atoms on the aryl ring with fluorine atoms, **JM10**, reverses the direction of the molecular dipole. The strong electron-withdrawing nature of the fluorinated ring induces a dramatic change in the direction of the dipolar moment, but some components of the dipole moment are, however, canceled by opposite contributions from the fluorine atoms aligned in the same direction. In contrast, replacing the perfluorinated aryl ring with two *meta*-positioned  $-\text{CF}_3$  groups in the aryl ring, as in **JM12**, diminishes this neutralization effect, increasing the molecular polarization and resulting in the highest net dipole moment among all the studied derivatives. Based on the estimated dipole moments of the different fullerene derivatives, it is expected that the synthesized fullerene derivatives exhibit strong interactions with the surface of the ionic perovskite structure. These electrostatic interactions are likely to facilitate the surface passivation by occupying under-coordinated ions and reducing the vacancy defects. Thus, an effective reduction of the trap-state density at the perovskite/ETL interface is expected for **JM10** and **JM12**, especially for the latest.<sup>46,47</sup>

To assess the impact of the interlayers deposition on the Sn perovskite film quality, X-ray diffraction (XRD) measurements and scanning electron microscopy (SEM) imaging were conducted, see Fig. S9 and S10.† The XRD patterns revealed two dominant peaks corresponding to the crystalline planes (100) and (200), indicating a clear preferential oriented growth along the (100) crystalline direction. The absence of any shift in the peak positions or significant changes in the full width at half-maximum (FWHM) values upon the interlayer deposition indicates that they do not disrupt the perovskite crystalline lattice. On the other hand, SEM images were taken at different magnifications and demonstrated the formation of uniform, pinhole-free layers with an average grain size exceeding 1  $\mu\text{m}$  in diameter in all the cases. Low-magnification SEM images suggested the presence of some organic material on the perovskite layer, with a noticeable difference between the **JM10** and **JM12** layers. Specifically, the **JM12** layer appeared more homogeneous, whereas the **JM10** layer showed more isolated organic domains. Apart from these differences in the interlayer homogeneity, minimal variations in the perovskite film morphology were observed, thus confirming the interlayer's compatibility with the  $\text{FASnI}_3$  perovskite and the high quality of the resulting films. To further study the interlayers homogeneity, atomic force microscopy (AFM) images were conducted. As shown in Fig. 2a–c, the **JM10** layer presented a non-uniform distribution with self-aggregate domains, whereas the **JM12** layer displayed a smooth and regular structure. This discrepancy between both materials can be attributed to a higher packing degree in the **JM10** layer, likely due to greater  $\pi$ – $\pi$  stacking interactions.<sup>48,49</sup>

A key limitation of Sn-PSCs is their voltage losses, mainly resulting from the non-radiative recombination and the misaligned energy levels at the top interface. The use of proper additives has significantly contributed to the reduction of bulk non-radiative recombination.<sup>10,29,50–52</sup> However, energy level misalignment has received less attention. To evaluate the charge extraction ability of the fullerene derivatives, Kelvin Probe Force Microscopy (KPFM) measurements were carried out. Fig. 2d shows the KPFM map of the pristine perovskite film, where higher values in the potential difference are observed at the grain boundaries. These sites can easily trap charge carriers due to the presence of structural defects, hindering their mobility and complicating their extraction to the ETL.<sup>53,54</sup> When the **JM10** layer is incorporated, as shown in Fig. 2e, a clear increase in the overall surface potential difference is observed, especially in the areas where the presence of the organic material is more prominent. Conversely, upon the addition of the **JM12** interlayer, a more uniform and complete perovskite coverage was obtained and the surface potential difference increased up respect both pristine and with **JM10** incorporation, as shown in Fig. 2f. These notable increases in the surface potential difference can be ascribed to an electron transport from the perovskite layer to the **JM12** fullerene derivative interlayer, demonstrating a huge potential to enhance the device performance, and confirming the difference in homogeneity between the organic layers previously commented.

To further explore the carrier dynamics and the interfacial recombination, steady-state photoluminescence (PL) and time-resolved photoluminescence (TRPL) spectroscopy measurements were performed for the  $\text{FASnI}_3/\text{C}_{60}$ ,  $\text{FASnI}_3/\text{JM10}/\text{C}_{60}$ , and  $\text{FASnI}_3/\text{JM12}/\text{C}_{60}$  samples. The PL spectra are shown in Fig. 2g, and a clear increase in PL intensity is observed upon the addition of both fullerene derivatives. A PL intensity enhancement is typically related to lower non-radiative recombination.<sup>55</sup> This increase can be ascribed to an effective surface passivation, reducing the non-radiative recombination centers at the top perovskite interface. Note that, as these samples are measured in open-circuit conditions, there is no net electron transfer from the perovskite to the charge transport layers during the steady-state PL measurements. Thereby, the effectiveness of charge extraction at the contacts cannot be directly inferred from these measurements, as sometimes assumed in literature.<sup>56</sup> However, in TRPL measurements, due to the transient nature of the technique substantial currents can flow to equilibrate the quasi-Fermi levels during the decay process. As a result, in addition to interface and bulk recombination, charge extraction processes must also be considered in TRPL experiments.<sup>57</sup>

The TRPL spectra are presented in Fig. 2h. PL decays have been fitted using a monoexponential decay function, obtaining average lifetimes ( $\tau_{\text{ave}}$ ) of 3.25 ns, 3.67 ns and 2.50 ns for  $\text{FASnI}_3/\text{C}_{60}$ ,  $\text{FASnI}_3/\text{JM10}/\text{C}_{60}$ , and  $\text{FASnI}_3/\text{JM12}/\text{C}_{60}$ , respectively. Interestingly, the trend observed in the steady-state PL between the sample with **JM12** and the reference is now reversed, with the **JM12** treated film showing a shorter  $\tau_{\text{ave}}$ . Considering that charge transport processes can occur in TRPL, the reduced  $\tau_{\text{ave}}$  observed for the sample with **JM12** can be attributed to an improved charge extraction from the perovskite layer to **JM12**,





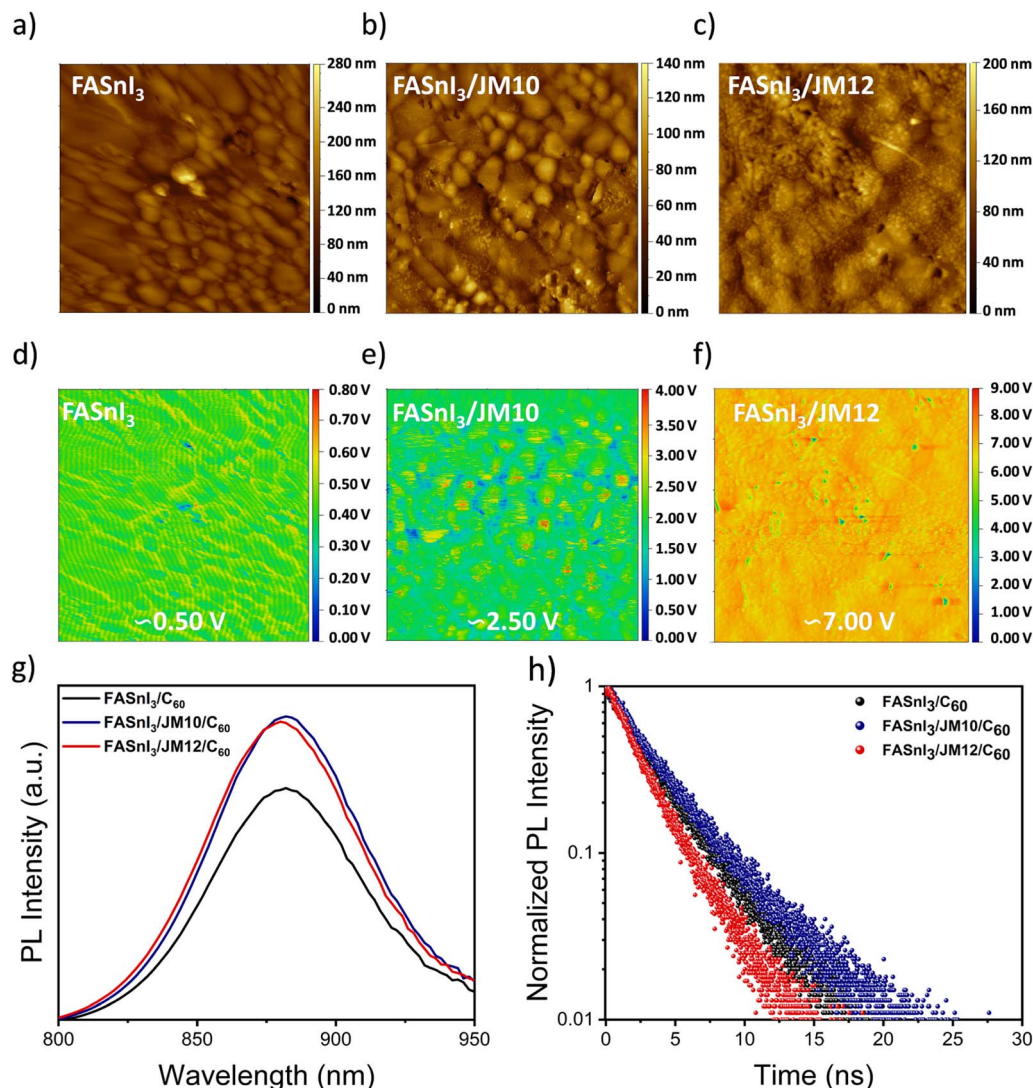


Fig. 2 AFM images of (a) FASnI<sub>3</sub>, (b) FASnI<sub>3</sub>/JM10 and (c) FASnI<sub>3</sub>/JM12 film surfaces. KPFM topography map of (d) FASnI<sub>3</sub>, (e) FASnI<sub>3</sub>/JM10 and (f) FASnI<sub>3</sub>/JM12 film surfaces. (g) PL spectra and (h) time-resolved PL decays corresponding to FASnI<sub>3</sub>/C<sub>60</sub> films on glass substrate with and without top interlayers.

while its higher steady-state PL emission indicates lower non-radiative recombination.

On the other hand, the FASnI<sub>3</sub>/JM10/C<sub>60</sub> sample exhibited the longest  $\tau_{\text{ave}}$  among all the samples. Here the trade of between the decrease of non-radiative recombination observed by steady PL, that causes an increase of  $\tau_{\text{ave}}$ , and the increase of charge extraction, producing a decrease of  $\tau_{\text{ave}}$ , should be considered. Thus, when comparing JM10 and JM12, both showed similar enhanced PL intensities, but the longer  $\tau_{\text{ave}}$  displayed by JM10 suggests less efficient charge extraction than for JM12.

To assess the ability of the interlayers to reduce the trap-state density ( $N_t$ ) in the perovskite film, we characterized the space-charge limited current (SCLC) of the devices.<sup>58,59</sup> As electrons are minority carriers in p-doped Sn-based perovskites, we fabricated electron-only devices with the structure of ITO/SnO<sub>2</sub>/FASnI<sub>3</sub>/C<sub>60</sub>/BCP/Ag with and without the interlayers between

perovskite and C<sub>60</sub>. The dark  $J$ - $V$  curves are presented in Fig. S10.† Commonly, three different regions can be distinguished, such as the ohmic region at low voltages, the trap-filled limited (TFL) region at intermediate voltages, and the Child region at high applied voltages. The intersection point between the ohmic and the TFL regions represents the trap-filled limit voltage ( $V_{\text{TFL}}$ ), where all the available trap states are completely filled by the injected carriers. Accordingly, the  $N_t$  can be calculated from the following equation:

$$N_t = \frac{2\varepsilon_r\varepsilon_0 V_{\text{TFL}}}{qL^2}$$

where  $L$  is the thickness of the perovskite film,  $\varepsilon_0$  is the vacuum permittivity,  $\varepsilon_r$  is the relative dielectric constant, and  $q$  is the elementary charge. The  $V_{\text{TFL}}$ 's of the control devices, as well as those incorporating JM10 or JM12, were estimated to be 0.148 V, 0.141 V, and 0.132 V, respectively. Therefore, these values



corresponded to the calculated  $N_t$  of  $9.17 \times 10^{15}$ ,  $8.74 \times 10^{15}$  and  $8.18 \times 10^{15} \text{ cm}^{-3}$ , respectively, confirming the ability of the interlayers to effectively passivate the interface between Sn-perovskite and  $\text{C}_{60}$ .

To further understand the chemical interactions behind the passivation mechanism of the perovskite surface by the interlayers, X-ray photoelectron spectroscopy (XPS) was performed. Changes in the local chemical environments of the different atoms present at the perovskite surface can be reflected through shifts in the binding energy peak positions. Fig. 3a shows the high-resolution Sn 3d XPS spectra, where the characteristic spin-orbit splitting of Sn 3d<sub>5/2</sub> and Sn 3d<sub>3/2</sub> is observed in the pristine  $\text{FASnI}_3$  perovskite, both with and without **JM10** and **JM12** interlayers. No significant shift in the binding energy of the  $\text{Sn}^{2+}$  components was detected in the presence of **JM10**, reflecting a weak interaction with the perovskite. In contrast, **JM12** induced a small but still noticeable change in the

electronic density distribution around the Sn nuclei, showing a higher downshift of 0.13 eV. A downshift in the binding energy implies an increased electron density around the Sn nucleus, suggesting that uncoordinated  $\text{Sn}^{2+}$  sites can be electronically compensated by the adsorption of **JM12** molecules, thereby improving the charge distribution at the surface. Furthermore, the high-resolution N 1s XPS spectra were also analyzed and presented in Fig. 3b. In the pristine perovskite, a single component corresponding to  $\text{FA}^+$  cations ( $\text{C}=\text{NH}_2^+$ ) was detected at 400.12 eV. Interestingly, this peak remained unchanged upon the addition of **JM10**, whereas it shifted to 400.00 eV after adding **JM12** interlayer. Additionally, a new signal associated with C–NH<sub>2</sub> was also detected at 398.96 eV and 398.86 eV for **JM10** and **JM12**, respectively. The observed downshift suggests an effective charge compensation from the fullerenes to the formamidinium cations, while the detection of the new signals may be ascribed to a structural rearrangement

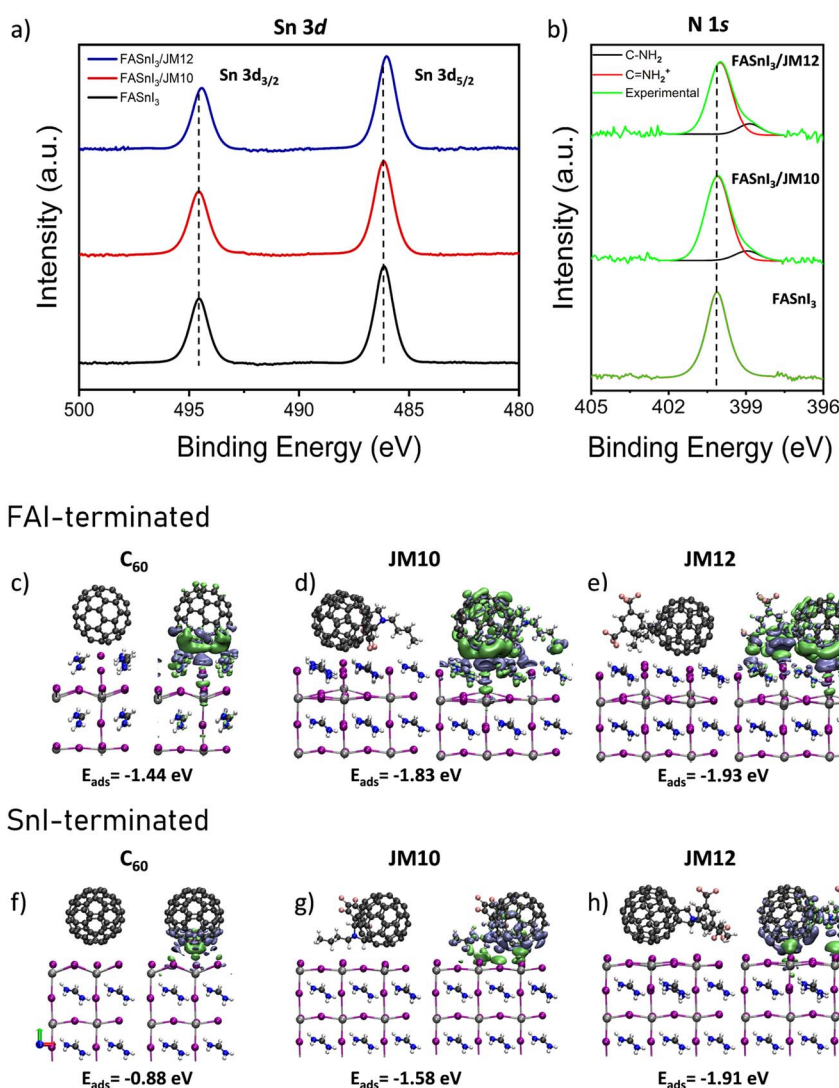


Fig. 3 High-resolution XPS spectra of (a) Sn 3d and (b) N 1s for the perovskite films with and without **JM10** and **JM12** interlayers. Isosurface of  $\Delta\rho = 0.002 \text{ a.u.}$  for (c and f)  $\text{FASnI}_3/\text{C}_{60}$ , (d and g)  $\text{FASnI}_3/\text{JM10}$ , and (e and h)  $\text{FASnI}_3/\text{JM12}$  systems with  $\text{SnI}_2$ -terminated and FAI-terminated structures, respectively. Green and blue regions represent positive and negative values of  $\Delta\rho$ , respectively.



or reorientation of the  $\text{FA}^+$  cations induced by the interaction with the fullerene derivatives.<sup>60</sup>

To validate this hypothesis, we performed DFT calculations to model the adsorption of the fullerene derivatives on different  $\text{FASnI}_3$  surfaces. We considered three distinct molecular orientations and two surface terminations, named  $\text{SnI}_2$ -terminated and FAI-terminated, see Fig. S12.† Since Sn-based perovskite surfaces are prone to irregularities and defect states which lead to heterogeneous atomic structures along the whole surface, considering all these scenarios can provide a more comprehensive and insightful analysis. All the calculated adsorption energies are summarized in Table S3.† Regarding the molecular orientation of the [60]fulleropyrrolidines, the adsorption energy was notably higher when both the fluorinated moiety and the fullerene cage interacted simultaneously with the surface, suggesting a preferred molecular orientation with multiple anchoring points, as shown in Fig. S13 and S14.† This dual interaction notably enhanced the adsorption, especially on FAI-terminated surfaces. Moreover, **JM12** exhibited higher adsorption energies than **JM10** in all cases, indicating that increasing the polarity of the electron-withdrawing substituent may enhance the adsorption stability, see Fig. 1d and Table S3.†

A more detailed analysis of the electron density changes for the cases with higher adsorption energies (*i.e.*, FAI-terminated surfaces and “middle” molecular orientations) showed an increase in electron density in the fullerene core for both in **JM10** and **JM12**, as shown in Fig. 3c–e, where green and blue regions represent areas of electron accumulation and depletion, respectively. This change is accompanied by a depletion of electron density at the interface, mainly due to electron donation from the external iodide atoms to the fullerene cage. Meanwhile, the regions where the fluorinated substituents directly interact with the perovskite surface exhibit an increase in electron density, particularly in the case of **JM12**. Thus, the formamidinium cation in the surface layer attracts electron density from the  $-\text{CF}_3$  groups in the aryl ring, reflecting the formation of strong interactions as previously observed in the XPS analysis, see Fig. 3b. Interestingly,  $\text{SnI}_2$ -terminated surfaces, where the external I atoms are missing, exhibited a different electron density redistribution upon molecular adsorption. As shown in Fig. 3f–h, an overall electron accumulation can be observed at the interface, compensating for the electron-deficient Sn sites and supporting the XPS results presented in Fig. 3a. Furthermore, although adsorption energies were stronger for FAI-terminated surfaces, the energy difference between **JM10** and **JM12** with  $\text{C}_{60}$  was significantly higher for  $\text{SnI}_2$ -terminated surfaces, highlighting the role of the fluorinated moieties in compensating charge-deficient sites. These findings not only corroborate the experimental results, but also provide useful information about the role of different molecular moieties in the electronic redistribution at the perovskite surface in different scenarios.

To study the potential of the interlayers to improve the performance of Sn-PSCs, we fabricated devices with an inverted p–i–n configuration following the architecture: ITO/PEDOT:PSS/ $\text{FASnI}_3/\text{C}_{60}$ /BCP/Ag, where PEDOT:PSS is poly(3,4-

ethylenedioxythiophene):polystyrene sulfonate and BCP is bathocuproine, see Fig. 4a. For the interlayer deposition, a 0.5 mM solution of **JM10** or **JM12** in chlorobenzene was dropped onto the perovskite film, see Fig. S15.† All the devices were exposed to a light-soaking treatment as part of a purification process, as previously reported by our group.<sup>29</sup> The photovoltaic parameters, including  $J_{\text{SC}}$ ,  $V_{\text{OC}}$ , fill factor (FF) and PCE are summarized in Fig. 4b, and the  $J$ – $V$  curves of the champion devices are also presented in Fig. 4c. The control devices exhibited a maximum PCE value of 9.4%, composed by a  $J_{\text{SC}}$  of  $22.4 \text{ mA cm}^{-2}$ , a  $V_{\text{OC}}$  of 0.63 V, and a FF of 68%. In contrast, the treated devices demonstrated enhanced maximum PCE values of 10.5% and 11.0%, with  $J_{\text{SC}}$  values of  $22.8 \text{ mA cm}^{-2}$  and  $22.6 \text{ mA cm}^{-2}$ ,  $V_{\text{OC}}$  of 0.68 V and 0.71 V, and FF of 67% and 68% for the **JM10** and **JM12** treated devices, respectively.

While the  $J_{\text{SC}}$  remained almost unchanged compared to the control devices, and the FF showed a slight improvement, the maximum increase was observed in the  $V_{\text{OC}}$  for the treated devices.  $V_{\text{OC}}$  is governed by the quasi-Fermi level splitting, influenced by recombination and transport layers' band alignment. Accordingly, impedance spectroscopy analysis was performed.<sup>61</sup> As shown in Fig. S16,† upon adding **JM10** and **JM12** a clear decrease in the recombination rate (higher recombination resistance) was observed, suggesting that the presence of the fullerenes reduces the global electronic recombination of the devices. The shallower LUMO levels of **JM10** and **JM12** also contributed to the higher  $V_{\text{OC}}$  observed. Interestingly, **JM10** presented a higher LUMO level, but its device performance did not match that of **JM12**, suggesting a better energy level transition for the latter. The superior performance of the **JM12** interlayer can also be attributed to lower non-radiative recombination of **JM12**, see Fig. 2g, and reduced trap state density, as determined by the SCLC measurements shown in Fig. S11.† This lower trap state density may indicate a more effective defect passivation with less non-radiative recombination sites. The smoother and more homogeneous morphology of **JM12** further supports this, as it provides a more uniform interface and may prevent the formation of deep trap states. In contrast, this effect seems to be less pronounced for the **JM10** interlayer, likely due to its more heterogeneous film. These findings also highlight the importance of material processability, which can allow for an efficient charge extraction while simultaneously enabling defect passivation at the interface. Eventually, the average FF of PSCs incorporating **JM12** showed an improvement (Fig. 4b) motivated by the enhanced charge extraction, see Fig. 2h.

Another major challenge that still needs to be addressed in Sn-PSCs involves their low stability specially under ambient conditions due to the deleterious effect of both oxygen and moisture.<sup>62</sup> In a previous report, we demonstrated that through adequate additive engineering, Sn-PSCs can show operational stabilities in  $\text{N}_2$  comparable to Pb-PSCs.<sup>29</sup> However, while it is not possible to completely prevent the degradation reactions triggered by oxygen and water molecules exposure, an adequate material design can significantly slow down these undesirable reactions. On this basis, we evaluated the operational stability of the unencapsulated devices in demanding ambient





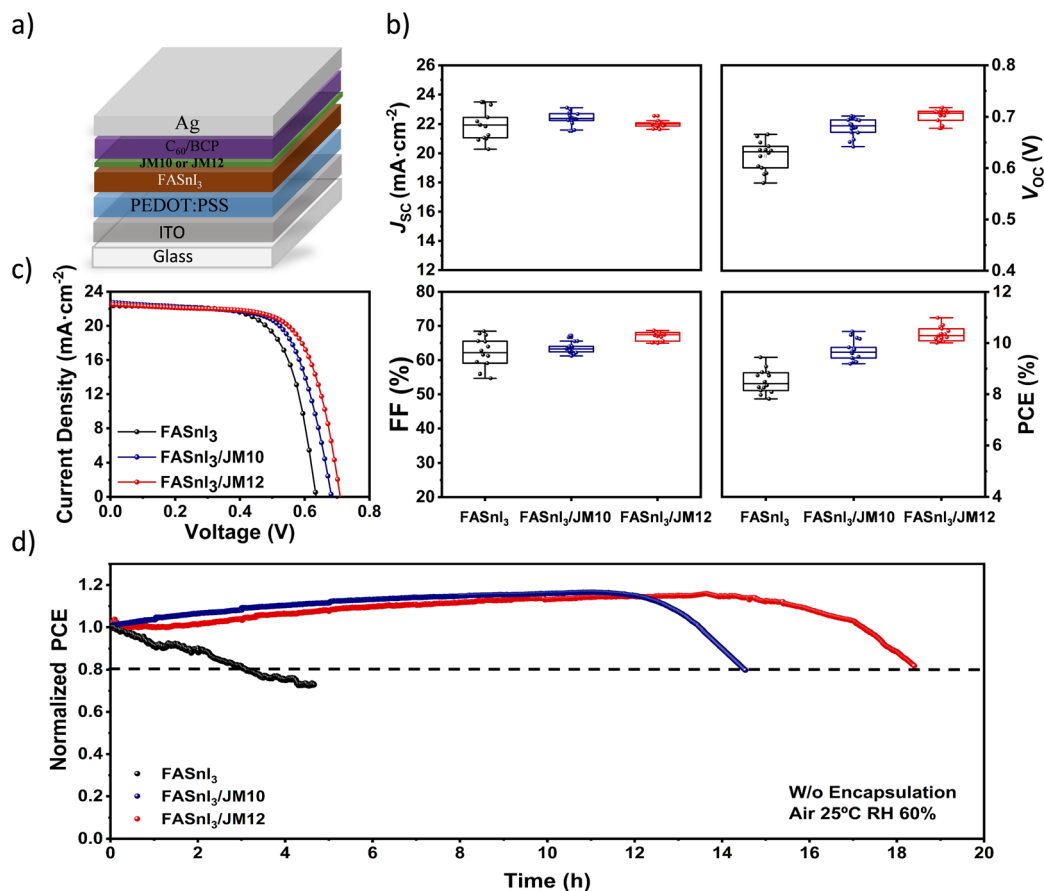
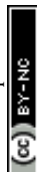


Fig. 4 (a) Sn-PSC device architecture, (b) statistics of the solar cell parameters including  $J_{SC}$ , FF,  $V_{OC}$  and PCE. All the parameters were extracted from J–V curves under  $100 \text{ mW cm}^{-2}$  AM 1.5G illumination. (c) Best performing devices' J–V curves. (d) MPP measurements for the control devices and for devices incorporating **JM10** and **JM12** in air without any encapsulation.

conditions (60% RH and  $25^\circ\text{C}$ ), tracking their performance at maximum power point (MPP) under continuous illumination ( $100 \text{ mW cm}^{-2}$ , AM 1.5G) at constantly applied voltages of 0.39 V, 0.40 V and 0.41 V for the control devices, and with **JM10** and **JM12** interlayers, respectively (Fig. 4d). The control device experienced a fast degradation, with a  $T_{80}$  lifetime of 3.1 hours. Conversely, devices presenting **JM10** and **JM12** interlayers demonstrated significantly enhanced stabilities, achieving impressive  $T_{80}$  lifetimes of 15.5 and 18.4 hours, respectively, which are, as far as we know, among the highest reported operational stabilities for Sn-PSCs under ambient conditions so far. To put this achievement in context, in one of our previous works<sup>29</sup> we achieved Sn-PSCs that retained up to 6 hours of ambient stability and over 1300 hours at 1 sun illumination at MPP and under ambient and  $\text{N}_2$  atmosphere, respectively. Herein, we demonstrated a threefold improvement in the ambient  $T_{80}$  lifetime, anticipating an outstanding stability with proper encapsulation. This achievement is particularly significant because, although ETLs such as PCBM or ICBA have demonstrated to effectively enhance  $V_{OC}$  and even shelf stability under  $\text{N}_2$ , they rarely improve the operational stability at MPP. In contrast, most published MPP data involve devices

employing  $\text{C}_{60}$  as the ETL, making our approach a useful guideline to achieve highly stable Sn-PSCs.<sup>25,29,51,63–66</sup>

To study the hydrophobicity of the passivated layers, we performed water contact angle measurements. The contact angles were measured immediately after the deposition of a water droplet onto the perovskite film surface, with and without the different interlayers, and results are presented in Fig. S17.† A clear tendency was revealed in the order:  $\text{FASnI}_3 < \text{FASnI}_3/\text{JM10} < \text{FASnI}_3/\text{JM12}$ , with angle values of  $48.9^\circ$ ,  $53.0^\circ$ , and  $57.8^\circ$ , respectively. This trend confirms the effect of the fullerene derivatives as efficient hydrophobic barriers against moisture, and is in perfect agreement with the trend observed in the operational stability measurements conducted in air. These findings demonstrate that appropriate surface modification strategies with specific hydrophobic groups can effectively retard Sn-PSCs degradation, thereby contributing to their long-term operational stability. Furthermore, the higher hydrophobicity of the **JM12** layer compared to **JM10**, can be attributed to the formation of a more uniform and homogeneous layer, as corroborated by KPFM images. We attributed the enhanced air stabilities to a protective effect offered by the fluorinated interlayers, owing to the hydrophobic character conferred by their high fluorine content.





## Conclusions

One of the main challenges currently limiting the development of Sn-PSCs is the offset between the perovskite CB and the LUMO levels of the most employed charge transport layers. In this work, we designed and synthesized two novel fullerene derivatives, **JM10** and **JM12**, functionalized with different fluorinated moieties, and incorporated them as interlayers in Sn-PSCs to enhance device performance. These interlayers successfully alleviated the energy level misalignment at the perovskite/C<sub>60</sub> interface, resulting in a significant increase in  $V_{OC}$  and boosting the PCE of the devices. Experimental results showed that **JM10** achieved a maximum efficiency of 10.5%, while **JM12** demonstrated a higher boost in the efficiency up to 11.0%, corresponding to an enhancement of approximately 20% with respect to the reference devices. Through both theoretical and experimental evidence, the enhanced efficiency is attributed to the distinct structural and electronic characteristics of each derivative, which decrease non-radiative recombination and optimize charge transfer at the FASnI<sub>3</sub>/ETL interface.

Furthermore, devices incorporating the interlayers exhibited impressive operational stability, retaining up to 80% of their initial PCE after 15 and 18 hours of operation in air (25 °C, 60% RH) under 1 sun illumination at MPP without any encapsulation for **JM10** and **JM12**, respectively. As far as we know this is one of the highest reported stabilities for Sn-PSCs for these harsh ambient conditions considering Sn-PSCs. These improvements in the operational stability are attributed to the enhanced hydrophobicity conferred by the fluorine-rich interlayers, which retard the degradation at the interface. It is important to highlight that, although other fullerene derivatives such as ICBA often result in remarkably  $V_{OC}$  enhancements, they fail to increase, and even reduce, Sn-PSCs stability at MPP. In contrast, the derivatives studied here simultaneously increased both efficiency and operational stability.

Consequently, our findings beyond the results here reported, reveal that suitable molecular engineering of fullerene derivatives plays a crucial role in enhancing both the performance and stability of Sn-PSCs, highlighting the potential of fluorine-rich functionalized materials for the development of more efficient and stable devices, giving molecular design guidelines and consequently paving the way to highly stable Sn-PSCs.

## Data availability

Data for this article are available at zenodo.org repository at <https://doi.org/10.5281/zenodo.15343587>.

## Author contributions

S. G.-L., I. M.-S. and J. L. D. conceived the idea. I. M.-S. and J. L. D. supervised the research. J. M.-G. synthesized the fullerene derivatives. S. G.-L. and J. S.-D. fabricated the solar cell devices and performed the characterization. N. G. contributed with the cyclic voltammetry experiments. J. P. M.-P. carried out the PL and TRPL measurements. J. S. performed the water contact

angle measurements. J. R.-P. conducted the XPS measurements. J. L.-T. and S. D.-T. executed the DFT calculations. E. M. B. carried out the AFM and KPFM experiments and contributed with the impedance spectroscopy interpretation. S. G.-L. prepared the first draft of the manuscript. J. P. and B. J.-L. contributed with the revision of the manuscript. I. M.-S. coordinate the final manuscript version. All the authors are involved in the discussion on data analysis and contributed to manuscript preparation.

## Conflicts of interest

There are no conflicts to declare.

## Acknowledgements

The financial support from the Ministry of Education, Youth and Sports of the Czech Republic for the XPS in the CEMNAT large research infrastructure (LM2023037) is gratefully acknowledged. J. L.-T. and S. D.-T. acknowledge the generous allocation of computer time at the Centro de Computación Científica at the Universidad Autónoma de Madrid (CCC-UAM). S. D.-T. acknowledges the MICINN – Spanish Ministry of Science and Innovation, Project PID2022-138470NB-I00, and the ‘María de Maeztu’ (CEX2023-001316-M) Program for Centers of Excellence in R&D, funded by MCIN/AEI/10.13039/501100011033. J. P. acknowledges support from Energy for the Future – E4F Postdoctoral fellowship program H2020-MSCA-COFUND-2020 (101034297). J. L. D. acknowledges Ikerbasque, Basque Foundation for Science, for an ‘Ikerbasque Research Associate’ contract, the Polymat Foundation, and the Spanish Government (PID2021-129084OB-I00, RED2022-134344-T). J. L. D. acknowledge support from the María de Maeztu Excellence Unit CEX2023-001303-M funded by MCIN/AEI/10.13039/501100011033. The authors acknowledge financial support for project PRINT-P (MFA/202/020) that forms part of the Advanced Materials program and was supported by MCIN with funding from European Union NextGenerationEU (PRTR-C17.I1) and by Generalitat Valenciana.

## References

- 1 A. Kojima, K. Teshima, Y. Shirai and T. Miyasaka, Organometal Halide Perovskites as Visible-Light Sensitizers for Photovoltaic Cells, *J. Am. Chem. Soc.*, 2009, **131**(17), 6050–6051.
- 2 H. Chen, C. Liu, J. Xu, A. Maxwell, W. Zhou, Y. Yang, Q. Zhou, A. S. R. Bati, H. Wan, Z. Wang, L. Zeng, J. Wang, P. Serles, Y. Liu, S. Teale, Y. Liu, M. I. Saidaminov, M. Li, N. Rolston, S. Hoogland, T. Filleter, M. G. Kanatzidis, B. Chen, Z. Ning and E. H. Sargent, Improved charge extraction in inverted perovskite solar cells with dual-site-binding ligands, *Science*, 2024, **384**(6692), 189–193.
- 3 S. Hu, J. Wang, P. Zhao, J. Pascual, J. Wang, F. Rombach, A. Dasgupta, W. Liu, M. A. Truong, H. Zhu, M. Kober-Czerny, J. N. Drysdale, J. A. Smith, Z. Yuan, G. J. W. Aalbers, N. R. M. Schipper, J. Yao, K. Nakano,



- S.-H. Turren-Cruz, A. Dallmann, M. G. Christoforo, J. M. Ball, D. P. McMeekin, K.-A. Zaininger, Z. Liu, N. K. Noel, K. Tajima, W. Chen, M. Ehara, R. A. J. Janssen, A. Wakamiya and H. J. Snaith, Steering perovskite precursor solutions for multijunction photovoltaics, *Nature*, 2025, **639**(8053), 93–101.
- 4 C. Yang, W. Hu, J. Liu, C. Han, Q. Gao, A. Mei, Y. Zhou, F. Guo and H. Han, Achievements, challenges, and future prospects for industrialization of perovskite solar cells, *Light: Sci. Appl.*, 2024, **13**(1), 227.
  - 5 WHO, *Exposure to Lead: A Major Public Health Concern*, World Health Organization, Geneva, 2010.
  - 6 J. Li, H.-L. Cao, W.-B. Jiao, Q. Wang, M. Wei, I. Cantone, J. Lü and A. Abate, Biological impact of lead from halide perovskites reveals the risk of introducing a safe threshold, *Nat. Commun.*, 2020, **11**(1), 310.
  - 7 N. Moody, S. Sesena, D. W. deQuillettes, B. D. Dou, R. Swartwout, J. T. Buchman, A. Johnson, U. Eze, R. Brenes, M. Johnston, C. L. Haynes, V. Bulović and M. G. Bawendi, Assessing the Regulatory Requirements of Lead-Based Perovskite Photovoltaics, *Joule*, 2020, **4**(5), 970–974.
  - 8 C. C. Stoumpos, C. D. Malliakas and M. G. Kanatzidis, Semiconducting Tin and Lead Iodide Perovskites with Organic Cations: Phase Transitions, High Mobilities, and Near-Infrared Photoluminescent Properties, *Inorg. Chem.*, 2013, **52**(15), 9019–9038.
  - 9 M. Konstantakou and T. Stergiopoulos, A critical review on tin halide perovskite solar cells, *J. Mater. Chem. A*, 2017, **5**(23), 11518–11549.
  - 10 J. Chen, J. Luo, Y. Li, X. Chen, Z. Song, E. Hou, C. Sun, H. Zhang, S. Cheng, Y. Xing, S. Chen, X. Zhao, L. Xie, C. Tian and Z. Wei, Spatially Isomeric Fulleropyrrolidines Enable Controlled Stacking of Perovskite Colloids for High-Performance Tin-Based Perovskite Solar Cells, *Angew. Chem., Int. Ed.*, 2025, **64**(7), e202420150.
  - 11 Y. Shi, Z. Zhu, D. Miao, Y. Ding and Q. Mi, Interfacial Dipoles Boost Open-Circuit Voltage of Tin Halide Perovskite Solar Cells, *ACS Energy Lett.*, 2024, **9**(4), 1895–1897.
  - 12 W. Shockley and H. J. Queisser, Detailed Balance Limit of Efficiency of p-n Junction Solar Cells, *J. Appl. Phys.*, 1961, **32**(3), 510–519.
  - 13 A. Filippetti, S. Kahmann, C. Caddeo, A. Mattoni, M. Saba, A. Bosin and M. A. Loi, Fundamentals of tin iodide perovskites: a promising route to highly efficient, lead-free solar cells, *J. Mater. Chem. A*, 2021, **9**(19), 11812–11826.
  - 14 S. Tao, I. Schmidt, G. Brocks, J. Jiang, I. Tranca, K. Meerholz and S. Olthof, Absolute energy level positions in tin- and lead-based halide perovskites, *Nat. Commun.*, 2019, **10**(1), 2560.
  - 15 L. Wang, Q. Miao, D. Wang, Z. Zhang, M. Chen, H. Bi, J. Liu, A. K. Baranwal, G. Kapil, Y. Sanehira, T. Kitamura, Q. Shen, T. Ma and S. Hayase, Ternary Passivation for Enhanced Carrier Transport and Recombination Suppression in Highly Efficient Sn-Based Perovskite Solar Cells, *Small*, 2024, **20**(46), 2404026.
  - 16 J. Jiménez-López, B. M. D. Puscher, D. M. Guldi and E. Palomares, Improved Carrier Collection and Hot Electron Extraction Across Perovskite, C<sub>60</sub>, and TiO<sub>2</sub> Interfaces, *J. Am. Chem. Soc.*, 2020, **142**(3), 1236–1246.
  - 17 P.-W. Liang, C.-C. Chueh, S. T. Williams and A. K. Y. Jen, Roles of Fullerene-Based Interlayers in Enhancing the Performance of Organometal Perovskite Thin-Film Solar Cells, *Adv. Energy Mater.*, 2015, **5**(10), 1402321.
  - 18 V. Georgakilas, J. A. Perman, J. Tucek and R. Zboril, Broad Family of Carbon Nanoallotropes: Classification, Chemistry, and Applications of Fullerenes, Carbon Dots, Nanotubes, Graphene, Nanodiamonds, and Combined Superstructures, *Chem. Rev.*, 2015, **115**(11), 4744–4822.
  - 19 R. C. I. MacKenzie, J. M. Frost and J. Nelson, A numerical study of mobility in thin films of fullerene derivatives, *J. Chem. Phys.*, 2010, **132**(6), 064904.
  - 20 F. Langa, P. de la Cruz, J. L. Delgado, M. J. Gómez-Escalonilla, A. González-Cortés, A. de la Hoz and V. López-Arza, The importance of the linking bridge in donor-C<sub>60</sub> electroactive dyads, *New J. Chem.*, 2002, **26**(1), 76–80.
  - 21 R. Sandoval-Torrientes, J. Pascual, I. García-Benito, S. Collavini, I. Kosta, R. Tena-Zaera, N. Martín and J. L. Delgado, Modified Fullerenes for Efficient Electron Transport Layer-Free Perovskite/Fullerene Blend-Based Solar Cells, *ChemSusChem*, 2017, **10**(9), 2023–2029.
  - 22 S. Collavini and J. L. Delgado, Fullerenes: the stars of photovoltaics, *Sustainable Energy Fuels*, 2018, **2**(11), 2480–2493.
  - 23 M. Zeng, Z. Yan, X. Ye, Y. Lou, T. Sheng, X. Jiang, Y. Mao, A. Huang, X. Yang, Z. Wang, Y. Sun, Y. Bai, H.-M. Cheng and G. Xing, Tailored Supramolecular Interface Enables Efficient and Stable Tin Halide Perovskite Photovoltaics, *ACS Energy Lett.*, 2025, 1357–1365.
  - 24 W. Liu, S. Hu, J. Pascual, K. Nakano, R. Murdey, K. Tajima and A. Wakamiya, Tin Halide Perovskite Solar Cells with Open-Circuit Voltages Approaching the Shockley–Queisser Limit, *ACS Appl. Mater. Interfaces*, 2023, **15**(27), 32487–32495.
  - 25 J. Chen, J. Luo, E. Hou, P. Song, Y. Li, C. Sun, W. Feng, S. Cheng, H. Zhang, L. Xie, C. Tian and Z. Wei, Efficient tin-based perovskite solar cells with trans-isomeric fulleropyrrolidine additives, *Nat. Photonics*, 2024, **18**(5), 464–470.
  - 26 B. Li, X. Wu, H. Zhang, S. Zhang, Z. Li, D. Gao, C. Zhang, M. Chen, S. Xiao, A. K. Y. Jen, S. Yang and Z. Zhu, Efficient and Stable Tin Perovskite Solar Cells by Pyridine-Functionalized Fullerene with Reduced Interfacial Energy Loss, *Adv. Funct. Mater.*, 2022, **32**(39), 2205870.
  - 27 Y. Bai, Q. Dong, Y. Shao, Y. Deng, Q. Wang, L. Shen, D. Wang, W. Wei and J. Huang, Enhancing stability and efficiency of perovskite solar cells with crosslinkable silane-functionalized and doped fullerene, *Nat. Commun.*, 2016, **7**(1), 12806.
  - 28 G. Nasti and A. Abate, Tin Halide Perovskite (ASnX<sub>3</sub>) Solar Cells: A Comprehensive Guide toward the Highest Power Conversion Efficiency, *Adv. Energy Mater.*, 2020, **10**(13), 1902467.



- 29 J. Sanchez-Diaz, R. S. Sánchez, S. Masi, M. Krečmarová, A. O. Alvarez, E. M. Barea, J. Rodriguez-Romero, V. S. Chirvony, J. F. Sánchez-Royo, J. P. Martínez-Pastor and I. Mora-Seró, Tin perovskite solar cells with >1,300 h of operational stability in N<sub>2</sub> through a synergistic chemical engineering approach, *Joule*, 2022, **6**(4), 861–883.
- 30 G. Li, Z. Su, L. Canil, D. Hughes, M. H. Aldamasy, J. Dagar, S. Trofimov, L. Wang, W. Zuo, J. J. Jerónimo-Rendon, M. M. Byrnavand, C. Wang, R. Zhu, Z. Zhang, F. Yang, G. Nasti, B. Naydenov, W. C. Tsoi, Z. Li, X. Gao, Z. Wang, Y. Jia, E. Unger, M. Saliba, M. Li and A. Abate, Highly efficient p-i-n perovskite solar cells that endure temperature variations, *Science*, 2023, **379**(6630), 399–403.
- 31 M. Jeong, I. W. Choi, E. M. Go, Y. Cho, M. Kim, B. Lee, S. Jeong, Y. Jo, H. W. Choi, J. Lee, J.-H. Bae, S. K. Kwak, D. S. Kim and C. Yang, Stable perovskite solar cells with efficiency exceeding 24.8% and 0.3-V voltage loss, *Science*, 2020, **369**(6511), 1615–1620.
- 32 S. Valero, T. Soria, N. Marinova and J. L. Delgado, Efficient and stable perovskite solar cells based on perfluorinated polymers, *Polym. Chem.*, 2019, **10**(42), 5726–5736.
- 33 X. Jiang, G. Yang, B. Zhang, L. Wang, Y. Yin, F. Zhang, S. Yu, S. Liu, H. Bu, Z. Zhou, L. Sun, S. Pang and X. Guo, Understanding the Role of Fluorine Groups in Passivating Defects for Perovskite Solar Cells, *Angew. Chem., Int. Ed.*, 2023, **62**(45), e202313133.
- 34 T. Dong, J. Liao, H. Li, J. Li, H. Li, Z. Li, L. Tan, X. Chen and W. Zhang, Performance Optimization of Perovskite Solar Cells via Fluorinated Carbonyl Additives, *ACS Appl. Mater. Interfaces*, 2025, **17**(8), 12291–12298.
- 35 X. He, T. Wu, X. Liu, Y. Wang, X. Meng, J. Wu, T. Noda, X. Yang, Y. Moritomo, H. Segawa and L. Han, Highly efficient tin perovskite solar cells achieved in a wide oxygen concentration range, *J. Mater. Chem. A*, 2020, **8**(5), 2760–2768.
- 36 C. Wu, M. Zhang, M. Yin, J. Luo, L. Ding and F. Hao, Enhanced Interlayer Interactions in Tin Halide Perovskite Solar Cells with a Fluorinated Fullerene Derivative, *J. Phys. Chem. Lett.*, 2025, **16**(5), 1261–1266.
- 37 M. Maggini, G. Scorrano and M. Prato, Addition of azomethine ylides to C<sub>60</sub>: synthesis, characterization, and functionalization of fullerene pyrrolidines, *J. Am. Chem. Soc.*, 1993, **115**(21), 9798–9799.
- 38 O. Tsuge and S. Kanemasa, Recent Advances in Azomethine Ylide Chemistry, in *Advances in Heterocyclic Chemistry*, ed. A. R. Katritzky, Academic Press, 1989, vol. 45, pp. 231–349.
- 39 G. Zhang and C. B. Musgrave, Comparison of DFT Methods for Molecular Orbital Eigenvalue Calculations, *J. Phys. Chem. A*, 2007, **111**(8), 1554–1561.
- 40 J. L. Delgado, S. Filippone, F. Giacalone, M. Á. Herranz, B. Illescas, E. M. Pérez and N. Martín, Buckyballs, in *Polyarenes II*, ed. J. S. Siegel and Y.-T. Wu, Springer International Publishing, Cham, 2014, pp. 1–64.
- 41 T. Nakamura, T. Nagai, Y. Miyake, T. Yamada, M. Miura, H. Yoshida, Y. Kanemitsu, M. A. Truong, R. Murdey and A. Wakamiya, Single-isomer bis(pyrrolidino)fullerenes as electron-transporting materials for tin halide perovskite solar cells, *Chem. Sci.*, 2025, **16**(5), 2265–2272.
- 42 I. P. Romanova, A. V. Bogdanov, I. A. Izdelieva, V. A. Trukhanov, G. R. Shaikhutdinova, D. G. Yakhvarov, S. K. Latypov, V. F. Mironov, V. A. Dyakov, I. V. Golovnin, D. Y. Paraschuk and O. G. Sinyashin, Novel indolin-2-one-substituted methanofullerenes bearing long n-alkyl chains: synthesis and application in bulk-heterojunction solar cells, *Beilstein J. Org. Chem.*, 2014, **10**, 1121–1128.
- 43 M. Karakawa, T. Nagai, K. Adachi, Y. Ie and Y. Aso, Precise control over reduction potential of fulleropyrrolidines for organic photovoltaic materials, *RSC Adv.*, 2017, **7**(12), 7122–7129.
- 44 F. Nisic, A. Colombo, C. Dragonetti, A. Cominetti, A. Pellegrino, N. Perin, R. Po and A. Tacca, Novel Terthiophene-Substituted Fullerene Derivatives as Easily Accessible Acceptor Molecules for Bulk-Heterojunction Polymer Solar Cells, *Int. J. Photoenergy*, 2014, **2014**(1), 373497.
- 45 H. Li, B. Chang, L. Wang, Z. Wang, L. Pan, Y. Wu, Z. Liu and L. Yin, Surface Reconstruction for Tin-Based Perovskite Solar Cells, *ACS Energy Lett.*, 2022, **7**(11), 3889–3899.
- 46 M. Zhang, Q. Chen, R. Xue, Y. Zhan, C. Wang, J. Lai, J. Yang, H. Lin, J. Yao, Y. Li, L. Chen and Y. Li, Reconfiguration of interfacial energy band structure for high-performance inverted structure perovskite solar cells, *Nat. Commun.*, 2019, **10**(1), 4593.
- 47 Y. Wu, B. Chang, L. Wang, H. Li, L. Pan, Z. Liu and L. Yin, Intrinsic Dipole Arrangement to Coordinate Energy Levels for Efficient and Stable Perovskite Solar Cells, *Adv. Mater.*, 2023, **35**(18), 2300174.
- 48 S. Banerjee, Molecular dynamics study of self-agglomeration of charged fullerenes in solvents, *J. Chem. Phys.*, 2013, **138**(4), 044318.
- 49 X. Yang, J. K. J. van Duren, M. T. Rispens, J. C. Hummelen, R. A. J. Janssen, M. A. J. Michels and J. Loos, Crystalline Organization of a Methanofullerene as Used for Plastic Solar-Cell Applications, *Adv. Mater.*, 2004, **16**(9–10), 802–806.
- 50 S. Galve-Lahoz, J. Sánchez-Diaz, C. Echeverría-Arondo, J. Simancas, J. Rodríguez-Pereira, S.-H. Turren-Cruz, J. P. Martínez-Pastor, I. Mora-Seró and J. L. Delgado, Addressing ambient stability challenges in pure FASnI<sub>3</sub> perovskite solar cells through organic additive engineering, *J. Mater. Chem. A*, 2024, **12**(33), 21933–21943.
- 51 O. E. Solis, M. Mínguez-Avellán, P. F. Betancur, R. I. Sánchez-Alarcón, I. Rodríguez, J. P. Martínez-Pastor, T. S. Ripolles, R. Abargues and P. P. Boix, Adjusting the Crystallization of Tin Perovskites through Thiophene Additives for Improved Photovoltaic Stability, *ACS Energy Lett.*, 2024, **9**(11), 5288–5295.
- 52 M. Pitaro, L. Di Mario, J. Pinna, D. A. Acevedo-Guzmán, M. Neophytou, M. Kirkus, T. D. Anthopoulos, G. Portale, P. Rudolf and M. A. Loi, Bulk Defects Passivation of Tin Halide Perovskite by Tin Thiocyanate, *Carbon Energy*, 2025, e710.



- 53 H. Uratani and K. Yamashita, Charge Carrier Trapping at Surface Defects of Perovskite Solar Cell Absorbers: A First-Principles Study, *J. Phys. Chem. Lett.*, 2017, **8**(4), 742–746.
- 54 N. Adhikari, A. Dubey, D. Khatiwada, A. F. Mitul, Q. Wang, S. Venkatesan, A. Iefanova, J. Zai, X. Qian, M. Kumar and Q. Qiao, Interfacial Study To Suppress Charge Carrier Recombination for High Efficiency Perovskite Solar Cells, *ACS Appl. Mater. Interfaces*, 2015, **7**(48), 26445–26454.
- 55 C.-Y. Chen, F. Harata, R. Murdey and A. Wakamiya, Enhanced Power Conversion Efficiency in Tin Halide Perovskite Solar Cells with Zinc Iodide Interlayers, *ACS Energy Lett.*, 2024, **9**(12), 6039–6046.
- 56 M. Stollerfoht, V. M. Le Corre, M. Feuerstein, P. Caprioglio, L. J. A. Koster and D. Neher, Voltage-Dependent Photoluminescence and How It Correlates with the Fill Factor and Open-Circuit Voltage in Perovskite Solar Cells, *ACS Energy Lett.*, 2019, **4**(12), 2887–2892.
- 57 T. Kirchartz, J. A. Márquez, M. Stollerfoht and T. Unold, Photoluminescence-Based Characterization of Halide Perovskites for Photovoltaics, *Adv. Energy Mater.*, 2020, **10**(26), 1904134.
- 58 J.-J. Cao, Y.-H. Lou, W.-F. Yang, K.-L. Wang, Z.-H. Su, J. Chen, C.-H. Chen, C. Dong, X.-Y. Gao and Z.-K. Wang, Multifunctional potassium thiocyanate interlayer for eco-friendly tin perovskite indoor and outdoor photovoltaics, *Chem. Eng. J.*, 2022, **433**, 133832.
- 59 Q. Dong, Y. Fang, Y. Shao, P. Mulligan, J. Qiu, L. Cao and J. Huang, Electron-hole diffusion lengths > 175  $\mu\text{m}$  in solution-grown  $\text{CH}_3\text{NH}_3\text{PbI}_3$  single crystals, *Science*, 2015, **347**(6225), 967–970.
- 60 M. Yang, J.-Y. Qiao, Y. Zheng, L. Li and J.-J. Yang, Mechanistic Exploration of Determinants for the Fullerene@FASnI<sub>3</sub> Interface Stability: Surface Termination and Monovalent Cation Rotation, *J. Phys. Chem. A*, 2024, **128**(39), 8561–8569.
- 61 S.-M. Yoo, S. J. Yoon, J. A. Anta, H. J. Lee, P. P. Boix and I. Mora-Seró, An Equivalent Circuit for Perovskite Solar Cell Bridging Sensitized to Thin Film Architectures, *Joule*, 2019, **3**(10), 2535–2549.
- 62 L. Lanzetta, T. Webb, N. Zibouche, X. Liang, D. Ding, G. Min, R. J. E. Westbrook, B. Gaggio, T. J. Macdonald, M. S. Islam and S. A. Haque, Degradation mechanism of hybrid tin-based perovskite solar cells and the critical role of tin (IV) iodide, *Nat. Commun.*, 2021, **12**(1), 2853.
- 63 D. He, P. Chen, J. A. Steele, Z. Wang, H. Xu, M. Zhang, S. Ding, C. Zhang, T. Lin, F. Kremer, H. Xu, M. Hao and L. Wang, Homogeneous 2D/3D heterostructured tin halide perovskite photovoltaics, *Nat. Nanotechnol.*, 2025, **20**(6), 779–786.
- 64 X. Liu, T. Wu, J.-Y. Chen, X. Meng, X. He, T. Noda, H. Chen, X. Yang, H. Segawa, Y. Wang and L. Han, Templated growth of FASnI<sub>3</sub> crystals for efficient tin perovskite solar cells, *Energy Environ. Sci.*, 2020, **13**(9), 2896–2902.
- 65 T. Li, Z. Zhang, F. He, L. Deng, Y. Yang, X. Mo, Y. Zhan and J. Liang, Alleviating the Crystallization Dynamics and Suppressing the Oxidation Process for Tin-Based Perovskite Solar Cells with Fill Factors Exceeding 80 Percent, *Adv. Funct. Mater.*, 2023, **33**(51), 2308457.
- 66 H. Rao, Y. Su, G. Liu, H. Zhou, J. Yang, W. Sheng, Y. Zhong, L. Tan and Y. Chen, Monodisperse Adducts-Induced Homogeneous Nucleation Towards High-Quality Tin-Based Perovskite Film, *Angew. Chem., Int. Ed.*, 2023, **62**(33), e202306712.

